

PAPER View Article Online
View Journal | View Issue



Cite this: Nanoscale, 2022, 14, 6133

Metallic vs. semiconducting properties of quasione-dimensional tantalum selenide van der Waals nanoribbons†

We conducted a tip-enhanced Raman scattering spectroscopy (TERS) and photoluminescence (PL) study of quasi-1D TaSe_{3- δ} nanoribbons exfoliated onto gold substrates. At a selenium deficiency of $\delta \sim 0.25$ (Se/ Ta = 2.75), the nanoribbons exhibit a strong, broad PL peak centered around \sim 920 nm (1.35 eV), suggesting their semiconducting behavior. Such nanoribbons revealed a strong TERS response under 785 nm (1.58 eV) laser excitation, allowing for their nanoscale spectroscopic imaging. Nanoribbons with a smaller selenium deficiency (Se/Ta = 2.85, $\delta \sim 0.15$) did not show any PL or TERS response. The confocal Raman spectra of these samples agree with the previously-reported spectra of metallic TaSe3. The differences in the optical response of the nanoribbons examined in this study suggest that even small variations in Se content can induce changes in electronic band structure, causing samples to exhibit either metallic or semiconducting character. The temperature-dependent electrical measurements of devices fabricated with both types of materials corroborate these observations. The density-functional-theory calculations revealed that substitution of an oxygen atom in a Se vacancy can result in band gap opening and thus enable the transition from a metal to a semiconductor. However, the predicted band gap is substantially smaller than that derived from the PL data. These results indicate that the properties of van der Waals materials can vary significantly depending on stoichiometry, defect types and concentration, and possibly environmental and substrate effects. In view of this finding, local probing of nanoribbon properties with TERS becomes essential to understanding such low-dimensional systems.

Received 24th November 2021, Accepted 25th March 2022

DOI: 10.1039/d1nr07772d

rsc li/nanoscale

Introduction

Recent investigations of two-dimensional (2D) van der Waals materials have revealed new physics and demonstrated potential practical applications. ^{1–14} Starting with graphene ^{7–9} and spreading to a wide range of layered van der Waals

materials, 10-14 the isolation of individual atomic layers from their respective bulk crystals has led to several breakthrough discoveries. In contrast to graphene or transition metal dichalcogenides (TMDs) that yield quasi-2D samples upon exfoliation, TiS₃ and TaSe₃¹⁵⁻¹⁸ yield quasi-one-dimensional (1D) nanostructures. These materials belong to the group of the transition metal trichalcogenides (TMTs) MX₃ (where M = various transition metals; X = S, Se, Te). Stoichiometric TaSe₃ has a monoclinic structure $(P2_1/m)$ space group) with lattice constants $a = 10.402 \text{ Å}, b = 3.495 \text{ Å}, c = 9.829 \text{ Å}, and <math>\beta =$ 106.26°. 19,20 The atoms form triangular prismatic units with Se atoms at the vertices and Ta in the center, which is repeated along the b-axis to form continuous chains (Fig. 1 inset). The inter-chain Ta-Ta separation is shorter than intra-chain Ta-Ta separation. The inset in Fig. 1 shows the atomic structure of parallel chains revealing a quasi-1D geometry. 19,21,22 The quasi-1D atomic threads are bound weakly in bundles by van der Waals forces and other interchain interactions (Fig. S1†).

Mechanical exfoliation of the MX_3 crystals results not in the 2D layers but rather in the needle-like structures. In some

^aNano-Device Laboratory (NDL) and Phonon Optimized Engineered Materials (POEM) Center, Department of Electrical and Computer Engineering, University of California, Riverside, California 92521, USA. E-mail: fkargar@ece.ucr.edu https://balandingroup.ucr.edu/

^bHORIBA Scientific, Novato, California94949, USA

^cDepartment of Chemistry and Material Science and Engineering Program, University of California, Riverside, California 92521, USA

^aDepartment of Chemistry, University of Georgia, Athens, Georgia 30602, USA
^eLaboratory for Terahertz and Terascale Electronics, Department of Electrical and Computer Engineering, University of California, Riverside, California 92521, USA
^fCenter for Computational Materials Science, U.S. Naval Research Laboratory, Washington, DC 20375, USA

[†]Electronic supplementary information (ESI) available. See DOI: https://doi.org/10.1039/d1nr07772d

Paper Nanoscale

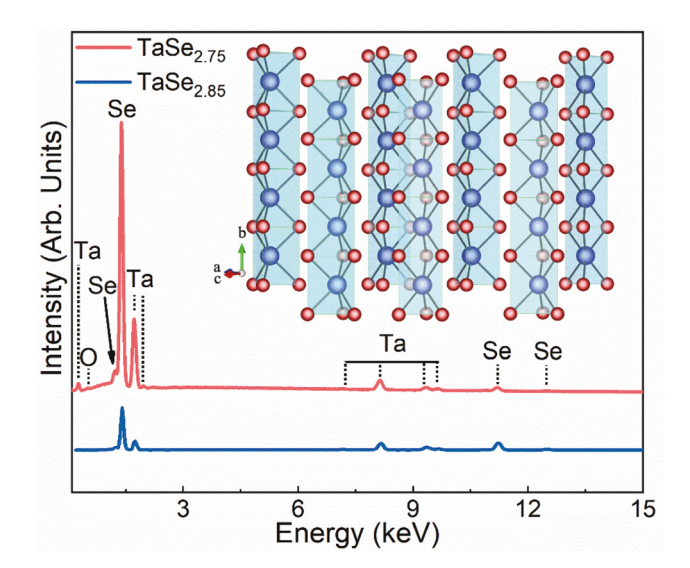


Fig. 1 Energy dispersive spectra of the synthesized and commercial ${\sf TaSe}_{3-\delta}$ crystals. The Se/Ta atomic ratio in the commercial sample is 2.75, indicating a larger Se deficiency compared to the CVT-grown crystal with a Se/Ta ratio of 2.85. The ${\sf TaSe}_{2.75}$ sample shows a weak peak, which is attributed to oxygen. The inset illustrates the crystal structure of quasi-1D ${\sf TaSe}_3$, with fused triangular prisms forming parallel chains along the b-axis. The red atoms represent Se and the blue ones indicate ${\sf Ta}$.

cases, the exfoliated samples are intermediate between the quasi-2D layers and quasi-1D nanowires. In the present study, the exfoliated $TaSe_{3-\delta}$ samples had a height in the range from 10 nm to 70 nm, and a width in the range from 100 nm to \sim 1 μ m. For this reason, we refer to them as nanoribbons. In our previous reports, we demonstrated that quasi-1D TaSe₃ nanoribbons could sustain a record high current density, $J_{\rm B}$ exceeding 30 MA cm⁻², which is an order of magnitude larger than that for the Cu nanowires. 18 The electronic transport characteristics and optical response of such TaSe3 nanoribbons were consistent with their metallic behavior, and in line with early reports of the properties of bulk TaSe₃ crystals. 18,23-26 However, some exfoliated quasi-1D nanoribbons of TaSe₃ have revealed current-voltage (I-V) characteristics and optical responses more typical for semiconductors. A recent study reported an observation of excitons in exfoliated bundles of TaSe₃.²⁷ It is rather unusual for metals to have excitons due to the high concentration of carriers and corresponding strong screening effects that disfavor exciton formation. These authors argued that dimensional confinement and strong many-body effects in bundles of quasi-1D metallic TaSe₃ result in exciton formation.²⁷

One should note that even the properties of bulk TaSe $_3$ are not yet fully understood. Because of the low superconducting transition temperature $T_{\rm C}\sim 2$ K, the bulk electrical characteristics of TaSe $_3$ have not been investigated as thoroughly as of some other TMTs. 19,20,28 Most studies reported that TaSe $_3$ crystals show metallic or semi-metallic behavior down to $T_{\rm C}$. 20,22,24,29 However, some studies indicated that stress or strain along the long axis can cause an appearance of a semi-

conducting gap. 30,31 Many reports on TaSe $_3$ crystals do not provide compositional or structural data, e.g., either energy-dispersive spectroscopy (EDS) or X-ray diffraction (XRD). For this reason, it is difficult to assess the composition and quality of the investigated materials. Selenium deficiency, corresponding to TaSe $_2$.8, has been observed in prior studies. 32,33 Rather unexpectedly, selenium deficiency in TaSe $_3$ has been reported even in selenium-rich CVT atmospheres. 30,34,35 Some studies of bulk crystals indicate that the background doping also can adjust the electronic structure of TaSe $_3$. 20,24,28,29,36 For example, as the sulfur content increases in the mixed TMT Ta ($S_xSe_{1-x})_3$, it becomes semiconducting, 37 while TaSe $_3$ with indium impurity exhibits a metal-to-insulator transition. 38,39 It was also reported that copper intercalation into TaSe $_3$ reduces T_C and weakens the charge-density-wave transitions. 40

Owing to the fast-growing interest in TMTs and other quasi-1D van der Waals materials, it is important to understand the fundamental nature of these materials, i.e., metallic vs. semiconducting, and to develop experimental approaches for inspecting the homogeneity or heterogeneity of properties at the nanoscale. In the present study, we show that selenium deficiency, combined with other possible effects, can change the behavior of TaSe3 nanoribbons from metallic to semiconducting. The differences in the optical response and electrical properties of the examined van der Waals ribbons suggest that even a small variation in the Se content can induce a change in material's behavior, making it appear more metallic or Our temperature-dependent semiconducting. electrical measurements indicate that the resistance of samples with higher Se deficiency decreases with increasing temperature, revealing a trend characteristic for semiconductors. The resistance of the samples with a composition closer to the stochiometric increases with temperature revealing a metallic behavior. Our findings may potentially explain some discrepancies in the reported characteristics of exfoliated nanoribbons of TaSe₃. Our results attest that a combination of tip-enhanced Raman spectroscopy (TERS), confocal Raman spectroscopy, and photoluminescence (PL) spectroscopy constitutes an effective nanometrology approach for characterization of nanostructures made from van der Waals materials. This capability is important for verification of the properties of numerous quasi-1D van der Waals materials predicted by machine learning studies, which are presently being synthesized. 41,42

Materials and methods

The bulk ${\rm TaSe}_{3-\delta}$ crystals for this study were grown by chemical vapor transport (CVT) or acquired from a commercial vendor (HQ Graphene; also, CVT grown). The details of the CVT synthesis have been reported by some of us elsewhere 18,43,44 and are not reproduced here. The in-house grown and commercial crystals selected for this study have consistent energy-dispersive X-ray spectroscopy (EDS) characteristics (see Fig. 1). The primary observable difference between the EDS data of ${\rm TaSe}_{3-\delta}$ samples are the selenium

Table 1 EDS characterization of the TaSe_{3- δ} crystals used in this study

	Ta (at. %)	Se (at. %)	Ratio Se/Ta
Theoretical	25.00	75.00	3.00
In-house grown crystal	26.00	74.00	2.85
Commercial crystal	26.69	73.31	2.75

content and a small peak attributed to the presence of oxygen atoms in TaSe_{2.75} samples. As summarized in Table 1, quantitative EDS characterization provides Se/Ta ratios of 2.85 for CVT-grown crystals and 2.75 for commercial crystals, which correspond to experimental compositions of TaSe_{2.85} and TaSe_{2.75}, respectively. The crystals were exfoliated to the template-stripped gold substrates, which were detached from the carrier wafer before the $TaSe_{3-\delta}$ exfoliation. We considered two sets of samples - nanoribbons of TaSe2.75 and nanoribbons of TaSe_{2.85}. The exact dimensions and geometries of the samples were determined by atomic force microscopy (AFM). The AFM, confocal Raman, and TERS characterization were performed using the XploRA-Nano AFM-Raman system (HORIBA Scientific) with the 100× and 0.70 NA side objective inclined at 65° with respect to the normal to the sample's surface. The 785 nm laser excitation with ~400 µW power on the sample surface was used for both the conventional confocal Raman and TERS measurements. The confocal Raman measurements were conducted using DualTwoPassTM mode with Access-SNC-Au TERS probes (Applied Nanostructures Inc.). Our TERS measurement procedures have been reported elsewhere. 45,46

Results and discussion

Fig. 2(a-b) and (c-d), shows the AFM images and scans of two representative exfoliated samples of $TaSe_{3-\delta}$ with $\delta \sim 0.25$ and $\delta \sim 0.15$, respectively. The first set of Raman measurements were conducted using TERS and confocal Raman on both types of samples shown in Fig. 2(a-d). As seen, the thicknesses of the examined samples are comparable. The spectroscopy results are shown in Fig. 2e. In this Figure, the blue and red curves are the confocal Raman and TERS spectra accumulated from TaSe_{2.75}. The TaSe_{2.85} samples did not reveal any TERS signal. Therefore, we show only the confocal Raman results of TaSe_{2.85} samples (dark cyan curve, Fig. 2e). There are several observations in this Figure that can be listed as follows. Firstly, comparing the spectra of confocal (blue curve) and TERS (red curve) spectra of TaSe_{2.75}, one would notice that the intensity of specific peaks, e.g., at 114 cm⁻¹ and 263 cm⁻¹, in the TERS spectrum is substantially enhanced compared to those observed in the confocal Raman spectrum. The TERS enhancement effect is closely related to the vibrational profile of atoms in those specific phonon modes. The reason for the observed enhancement will be discussed further. None of the exfoliated TaSe_{2.85} samples showed any TERS signal. The second observation is that there are intense Raman peaks at >270 cm⁻¹ in the TERS spectrum of TaSe_{2.75} (red curve) which are absent or

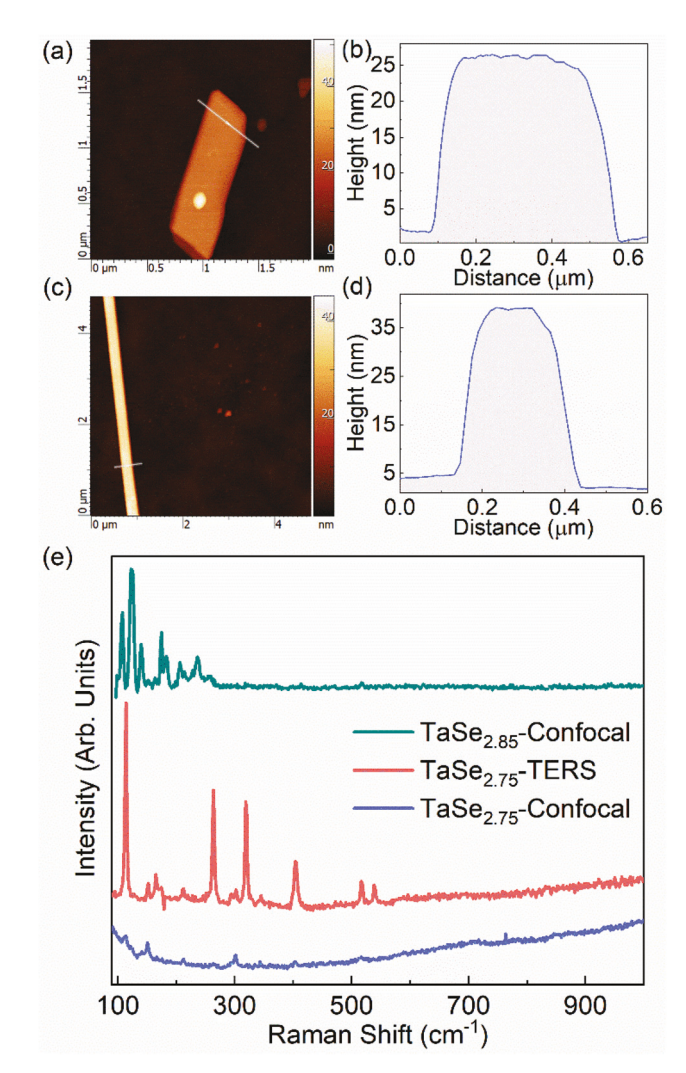


Fig. 2 AFM topography analysis of (a and b) TaSe $_{2.75}$ and (c and d) TaSe $_{2.85}$ nanoribbons. (e) TERS and confocal Raman spectra accumulated for the samples shown in panels (a) and (c). Exfoliated samples with higher Se deficiency exhibit TERS enhancement and high-order Raman modes with strong photoluminescence background (red and blue curves) whereas TaSe $_{2.85}$ samples exhibit neither of these characteristics.

very weak in the confocal Raman spectrum of the same crystal. These peaks are attributed to the high-order or multiphonon Raman scattering processes. These high wavenumber peaks are absent in the data accumulated for TaSe_{2.85} (cyan curve). A third observation is that the Raman spectra of TaSe_{2.75} samples are accompanied by an intense photoluminescence background, which is not seen in the spectrum collected for TaSe_{2.85}. This observation suggests that samples with larger Se deficiency possess semiconductor characteristics whereas samples with close to stoichiometric composition are metallic. We will address the photoluminescence in detail. Fourth, although the Raman spectra of the samples look superficially different in the range between 100 cm⁻¹ to 300 cm⁻¹, in fact both agree well with the calculations, with only the intensities of the peaks differing. TaSe₃ has many

Paper

Raman signatures, with closely-packed peaks that will be dis-

cussed in more details below. We focus here on the TERS data of TaSe_{2,75} given its more intense and well-defined spectral features.

Fig. 3a shows the AFM thickness analyses of the exfoliated TaSe_{2.75} sample used for TERS experiments. The AFM image is presented in the ESI Fig. S2.† Fig. 3b shows the intensity distribution of the most dominant Raman peaks at 265 cm⁻¹ (red color), 320 cm⁻¹ (blue color) and 405 cm⁻¹ (green color), respectively. Fig. S3† presents the same plot for each individual Raman peaks. The data were accumulated under 785 nm (1.58 eV) laser excitation at 400 µW power on the sample surface, and 1 second per pixel integration time. The map repeats the topography image of the exfoliated TaSe_{2.75} sample with high fidelity (compare with the AFM image presented in Fig. S2†). There is a sharp drop in the signal intensity at the edges of the crystal, which indicates the lack of significant far-field Raman contribution to the collected spectra. Interestingly, TERS spectra averaged over the darker stripes in the TERS map

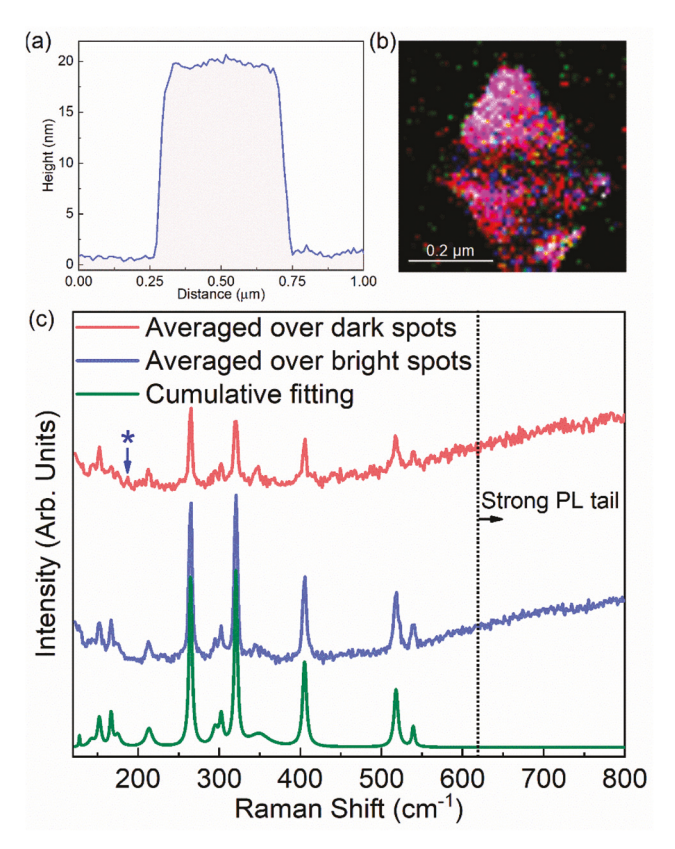


Fig. 3 (a) AFM topography analysis of the TaSe_{2.75} sample used in TERS measurement. (b) TERS contour map presenting the intensity distribution of Raman dominant peaks at 265 cm⁻¹, 320 cm⁻¹ and 405 cm⁻¹, respectively. (c) TERS spectra averaged over the bright (blue spectrum) and dim (red spectrum) areas in the TERS map presented in panel (b). The green curve shows the cumulative fitting over the experimental data using individual Lorentzian functions. The peak labeled with "*" belong to A_q vibrational symmetry and could not be fitted due to its low intensity.

showed not only an overall decrease in the signal intensity of the intense bands at 265 cm⁻¹, 320 cm⁻¹ and 405 cm⁻¹ but also a disproportionate decrease in the intensity and a slight red shift of the 166 cm⁻¹ and 540 cm⁻¹ (~1 cm⁻¹) bands. Fig. 3c shows the TERS of the same sample in the spectral range of 100-600 cm⁻¹. The data represents the averaged intensity of the peaks over the bright (blue curve) and dim (red curve) spots. The green curve is the cumulative fitting over the experimental data points using individual Lorentzian functions. In this spectrum, 14 Raman peaks are represented: at 127, 142, 152, 166, 174, 213, 264, 294, 302, 320, 349, 405, 517, and 539 cm⁻¹. A low-intensity peak at 187 cm⁻¹ could not be fit using the Lorentzian or other functions due to its low intensity. Furthermore, a series of confocal Raman measurements were conducted using special notch filters with the cut-off frequency at ~60 cm⁻¹. In this case, two other peaks at ~75 cm⁻¹ and 82 cm⁻¹ were identified (Fig. S4†).

As illustrated in Fig. 4a and reported by some of us previously,⁴⁷ the maximum energy of the optical phonons along all the high-symmetry directions fall below $\sim 270 \text{ cm}^{-1}$ [see ref. 47 and Fig. 4a] and those Raman peaks observed at higher frequencies than 270 cm⁻¹ belong to the high-order Raman scattering processes. The high-order Raman peaks are a measure of the phonon density of states (PDoS). 48,49 Momentum conservation in two-phonon scattering is satisfied when $q_1 \pm q_2 \sim$ 0 in which q_i , i = 1,2 is the wavevector of the specific phonon mode contributing to the scattering and plus and minus signs represent combination and difference modes. Therefore, the momentum conservation restrictions of single-phonon scattering do not apply in multi-scattering processes and basically, phonons satisfying the above condition may appear in the Raman spectrum. The details surrounding the selection rules for higher-order Raman scattering processes in $TaSe_{3-\delta}$ is beyond the scope of this investigation. The appearance of high-order Raman bands in TaSe_{2.75} with larger Se deficiency and their absence in TaSe2.85 indicates the role of defects and a possible change in the electronic band structure and optical properties. The significant change in the electronic band structure and bandgap opening as a result of defects can potentially cause Raman resonant scattering processes to take place. At resonant conditions, the high-order Raman peaks become more intense and visible, as reported previously in several material systems. 50,51 As seen in Fig. 3c, at higher wavenumbers >600 cm⁻¹, the Raman spectra are accompanied with a strong background attributed to the PL tail. In all experiments, the presence of the PL tail was accompanied consistently by the appearance of higher-order Raman modes, further indicating the role of Se deficiency or other defects in changing material's electronic properties from metallic to semiconductor.

To rationalize our experimental Raman data, we calculated the phonon dispersion and PDOS of stoichiometric TaSe₃ using the density functional theory (DFT). The results are presented in Fig. 4a. The red symbols represent our experimental Raman peaks for TaSe_{2.75}. As one can see, the experimental data points agree well with the theoretical calculations and the Nanoscale Paper

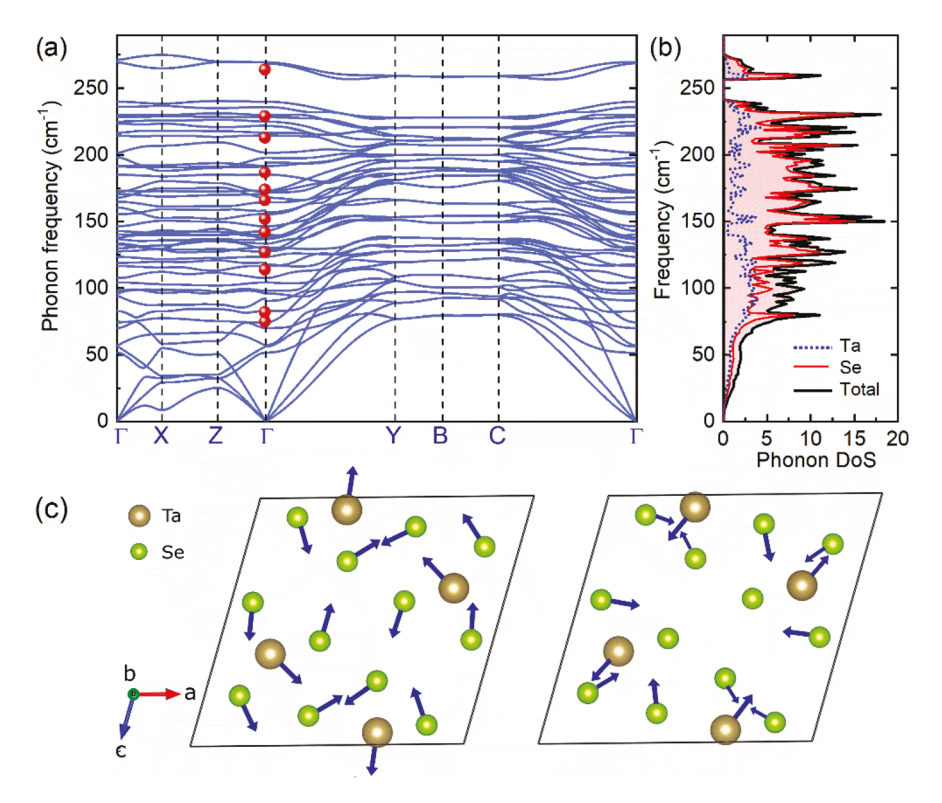


Fig. 4 (a) Phonon band structure, and (b) phonon density of states of stoichiometric TaSe_x. The red symbols are the experimental Raman peaks accumulated from TaSe_{2.75}. (c) vibrational profiles and symmetry of the Raman bands at 114 cm⁻¹ (left) and 263 cm⁻¹ (right) with strong displacement profile of atoms in the a-c plane. The intensity of these modes is preferentially enhanced in TERS measurements.

previously reported values. 47,52 Table S1 in the ESI† lists the spectral positions of the Raman peaks, theoretical calculations for the Brillouin zone center (Γ) , and the previously reported data in the literature. The unit cell of TaSe₃ has 16 atoms (see Fig. S1(a)†) with 45 optical phonon branches. This large number results in rich Raman response, illustrated in Fig. 3c. The vibrational symmetry of the atomic chain and the crystal are represented by: $\Gamma_{\text{TaSe}_3} = 8A_{\text{u}} + 8B_{\text{g}} + 16B_{\text{u}} + 16A_{\text{g}}$, where A_{g} and $B_{\rm g}$ modes are Raman active.⁵² The vibrational symmetry of Raman active modes is also included in Table S1.† We observed experimentally TERS enhancement of the Raman peaks at 114 cm⁻¹ and 263 cm⁻¹ (see Fig. 2e). These two peaks have Ag symmetry with strong displacement of atoms in the ac plane (see Fig. 4b). In TERS experiments, a strong electric field of the localized surface plasmons between the apex of the metallic gold tip and sample's surface intensifies Raman peaks owing to the 4th order dependence of the Raman intensity, I, on the magnitude of the local electric field (E), i.e., $I \sim$ E.4 The direction of the induced localized electric field lies along the normal to the sample's surface. Consequently, the Raman-active modes with the large atomic vibrational profiles and polarizability along the confined electric field are enhanced preferentially. Given that the peaks at 114 cm⁻¹ and 263 cm⁻¹ must have similar vibrational displacements in both TaSe_{2.75} and TaSe_{2.85}, one would expect that these modes should appear in the TERS spectra for both type of crystals with low and high Se deficiencies. However, the lack of any

TERS signal for TaSe_{2.85} samples suggests that their TERS response is suppressed by their metallic properties.

The increasing background in TERS spectra collected over the 20 nm thick nanoribbon suggest the presence of a PL peak tail (see spectra in Fig. 2e for >600 cm⁻¹). To determine the exact position of this PL peak, and to confirm that other exfoliated TaSe_{2.75} samples also show TERS response, we performed TERS and tip enhanced PL (TEPL) imaging of several nanoribbons and small samples of different geometries. We used the lower density grating in the Raman instrument to expand the covered spectral range in a single measurement. A broad PL peak with a maximum at approximately ~922 nm (1.34 eV) was present in both the TERS and conventional confocal Raman spectra collected over the same samples. To verify this observation, we conducted PL mapping on a 70 nm thick sample with larger lateral dimensions. The AFM image and thickness analysis of the sample are presented in the Fig. S5† and the inset of Fig. 5, respectively. The results of PL measurements are shown in Fig. 5. The PL peak at 922 nm is consistently present for the samples with larger Se deficiency ($\delta \sim$ 0.25). The strong PL response of this sample allowed us to use a short integration time of 20 ms per pixel and to collect a high pixel density PL map, which followed the topography image with high fidelity (Fig. S6†). In samples with lower Se deficiency ($\delta \sim 0.15$, the PL peak was not observed. This observation suggests the material's electronic characteristic can undergo substantial changes with varying Ta/Se proportions.

Paper Nanoscale

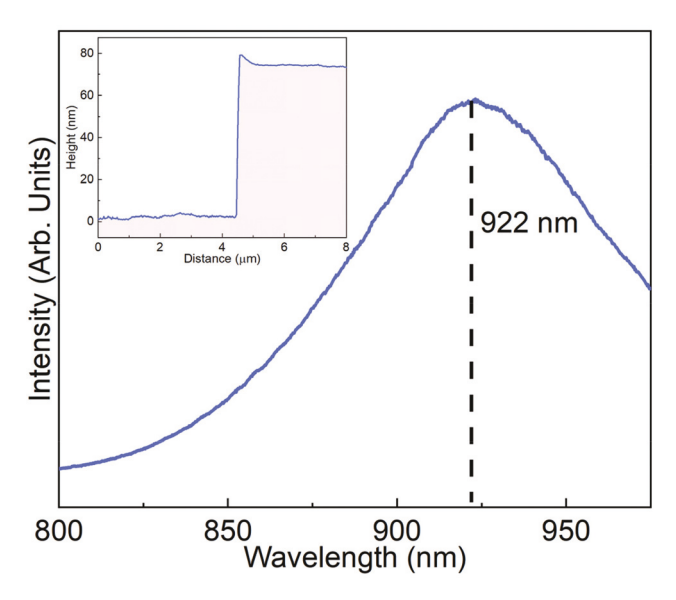


Fig. 5 PL spectrum averaged over the sample surface indicating the PL maximum at 922 nm (1.34 eV). The inset presents the AFM scan of the sample showing its thickness.

These results establish that TERS enhancement, the appearance of the high-order Raman modes, and the PL tail and peak can be used as tools to distinguish semiconducting vs. metallic samples of exfoliated TaSe_{3- δ}. As discussed above, most of the reported studies indicate metallic behavior by TaSe₃ in both transport and optical measurements.^{23–25} The examined CVT-grown TaSe2.85 nanoribbons did not show any PL or TERS enhancement response whereas TaSe_{2.75} exhibited both. For this reason, we hypothesized the differences in optical spectra can be related to the degree of selenium deficiency. The samples with the composition closer to the stoichiometric TaSe3 are more likely to be metallic. In order to verify this hypothesis, we fabricated devices with $TaSe_{3-\delta}$ channels and measured their I-V characteristics as a function of temperature. The results of such measurements for TaSe_{2.75} and TaSe_{2.85} are presented in Fig. 6(a and b). The insets in the figure show the SEM images of the tested devices. The resistance of the devices fabricated with TaSe2.75 decreases with temperature, whereas it increases for TaSe2.85 devices as the temperature increases. These trends confirm that the samples with larger Se deficiency reveal semiconducting behavior.

To explore the possibility of band-gap opening due to composition and defects, we theoretically investigated the effect of Se vacancies and Se/O substitution. We calculated the density of states (DOS) of the stoichiometric bulk TaSe₃ crystal, the Se deficient TaSe_{2.75} containing Se vacancies, and an O-substituted structure TaSe_{2.75}O_{0.25} using Density Functional Theory (DFT.)^{53,54} The stoichiometric TaSe₃ unit cell has 4 Ta atoms and 12 Se atoms. To create the Se deficient structure of TaSe_{2.75}, we removed one Se atom from the stoichiometric unit cell. Depending on the position of removed Se atom, two different configurations were considered, interchain and intrachain vacancies, as shown in Fig. 7. In the interchain configur

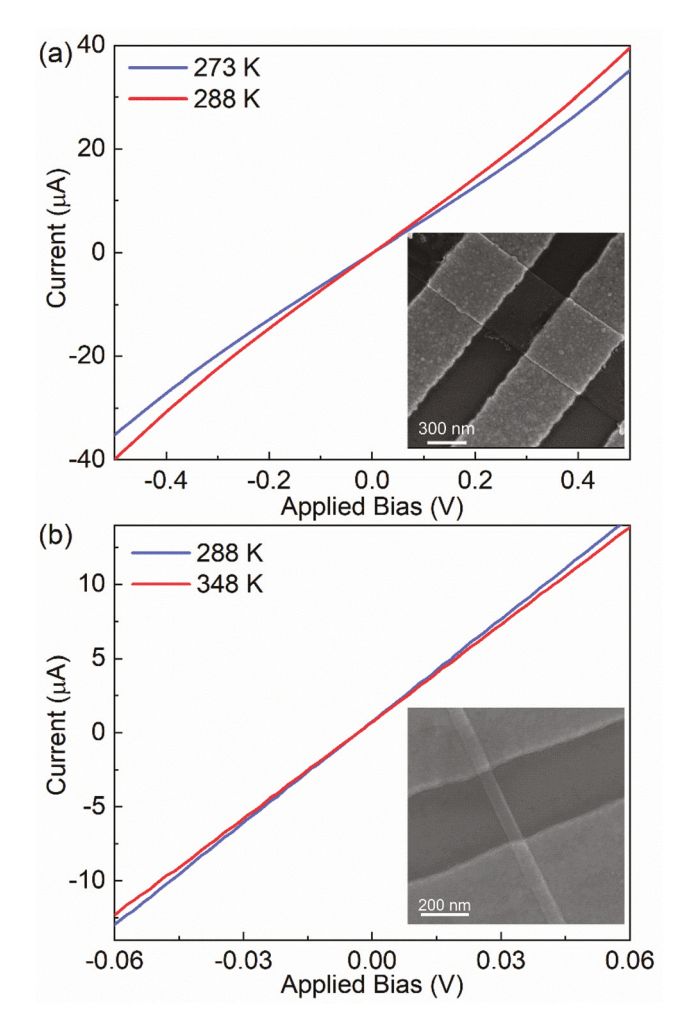


Fig. 6 I-V characteristics of devices with (a) TaSe_{2.75}, and (b) TaSe_{2.85} channels shown at two different temperatures. The electrical resistance of the devices with the TaSe_{2.75} and TaSe_{2.85} channels decreases and increases with temperature rise, respectively. This indicates a transition from semiconducting to metallic conduction depending on the degree of Se deficiency.

ation, a Se atom that connects two Ta atoms from adjacent chains is removed. In the intrachain configuration, a Se atom, connecting two Ta atoms of same chain, is removed. Due to the well-known oxidation of metal chalcogenides, we considered two more interchain and intrachain configurations, in which the Se vacancy is filled by oxygen.

Structure relaxation of all configurations were performed using the Vienna *ab initio* Simulation Package (VASP)⁵⁵ and the Python based atomic simulation environment (ASE).⁵⁶ We used the Perdew–Burke–Ernzenhof (PBE) exchange correlation (xc) functional⁵⁷ and a plane wave basis set with an energy cutoff at 500 eV to calculate the ground state energy of these materials. The DFT-D2 method proposed by Grimme⁵⁸ is included in these calculations to account for the van der Waals interaction. The structures were relaxed until the maximum force on all individual atoms was less than 0.1 meV A⁻¹. To investigate the effect of vacancies and O-substitution on

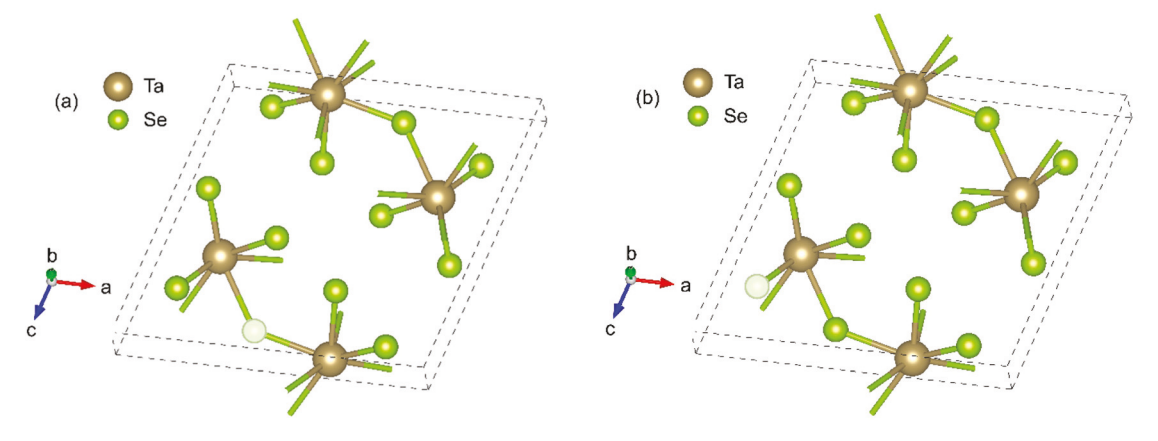


Fig. 7 (a) Interchain and (b) Intrachain vacancy configuration of TaSe_{2.75}. The twelve atoms within the unit cell are shown. The transparent spheres represent Se vacancies or O-substituted Se atoms.

bandgap, we calculated the density of states using the Heyd-Scuseria-Ernzerhof (HSE06) hybrid functional⁵⁶ without and with spin orbit coupling (SOC), since the SOC of both Ta and Se is large. The Brillouin zone was sampled with a $6 \times 14 \times 6$ Monkhorst-Pack k-point grid. Bulk phonon calculations of stoichiometric TaSe₃ were calculated as described previously.⁴⁷

Fig. 8 shows the HSE06-SOC DOS plots resulting from interchain and intrachain configurations for both the Se deficient and oxygen substituted structures. Fig. 8(a) shows the DOS with the Se vacancy, and Fig. 8(b) shows the DOS with O-substitution. The DOS plots without SOC are provided in Fig. S7.† The dashed black curves show the DOS of the stoichiometric structure. We first examine the DOS at the Fermi level of the vacancy structures. We find the DOS at the Fermi level for both the interchain and intrachain vacancy structures is larger compared to the DOS of the stoichiometric structure. The vacancy structures remain metallic and, therefore, we do not find a compelling case for Se vacancies leading to the energy bandgap extracted from the PL data.

The effect of O substituting for the Se sites gives a more consistent picture independent of the presence or absence of SOC. O substitution results in a small gap around the Fermi level with a larger gap for interchain substitution as we show in Fig. 8(b). The size of the gap, however, is relatively small, between 0.05 and 0.1 eV (depending on whether substitution is on the interchain versus intrachain site), which is approximately an order of magnitude less than the experimentally observed PL peak. The simulations show that the vacancies alone, with the concentrations in the considered range, cannot explain the observed optical response. Oxygen substitution can create an energy band gap but its magnitude remains relatively small. Interestingly, oxygen substitution for S atoms was reported to open up a bandgap in another material such as $TiS_{2-x}O_x$. It was found that the band gap monotonically increases with oxygen concentration.⁵⁹ In addition to the deviation from the stoichiometry and oxygenation, one should assume possible influence of other defects, environmental and substrate effects, e.g. strain, to

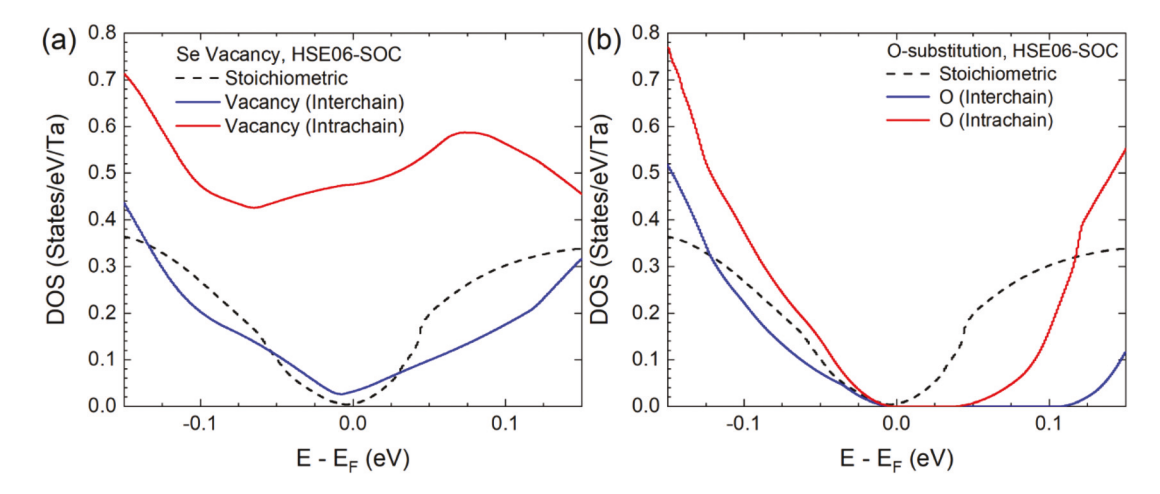


Fig. 8 Electronic density of states for (a) the Se deficient structure TaSe_{2.75}, (b) the oxygen substituted structure TaSe_{2.75}O when both HSE and SOC are taken into consideration.

Nanoscale Paper

explain experimentally observed differences in properties.

academia is a part of A.K. job responsibilities. There are no conflicts to declare.

Conclusions

We conducted a tip-enhanced Raman scattering spectroscopy and photoluminescence study of nanoribbons exfoliated from two quasi-1D TaSe_{3- δ} samples, with Se deficiency of $\delta \sim 0.15$ and $\delta \sim 0.25$. The TaSe_{2.75} nanoribbons exhibited strong, broad PL peak centered at 922 nm (1.34 eV) and TERS response under 785 nm laser excitation, consistent with semiconducting behavior. The TaSe_{2.85} nanoribbons showed neither PL nor TERS response, in agreement with the metallic characteristic of stochiometric TaSe₃. The confocal Raman spectra of ribbons of both types agreed well with the previously reported spectra of metallic TaSe₃. The temperature-dependent electrical measurements on two-terminal devices fabricated with nanoribbons of TaSe_{2.85} and TaSe_{2.75} indicated semiconducting and metallic trends, in line with the optical studies. The density-functional theory calculations of the electronic band structure suggested that oxygen substitution rather than Se vacancies can produce band gap opening in this system. Oxygen substitution results in a relatively small bandgap opening in the range of 0.05 to 0.1 eV. The calculated bandgap is an order of magnitude smaller than that experimentally observed in PL measurements. The differences in the optical response and electrical transport of the examined nanoribbons suggest that even small variations in Se content can induce changes in this material's behavior, making it appear metallic or semiconducting. This observation may explain some discrepancies in the earlier reported transport characteristics of exfoliated nanoribbons of TaSe3. Our results also attest that a combination of TERS and PL spectroscopy constitutes a powerful nanometrology tool for the characterization of nanostructures made from van der Waals materials.

Author contributions

A. A. B. coordinated the project and contributed to the data analysis. F. K. and A. K. conceived the idea of the study. Y. G. synthesized bulk crystals and conducted characterization. T. T. S. supervised material synthesis and contributed to data analysis. A. K. performed TERS measurements and contributed to data analysis. M. W. fabricated the test structures and conducted electrical measurements. L. B. supervised nanofabrication and contributed to data analysis. T. D. and D. W. performed the ab initio computational studies. R. K. L. supervised the computational studies and conducted theoretical analysis. All authors contributed to writing and editing of the manuscript.

Conflicts of interest

A portion of this research was done on HORIBA Scientific AFM-Raman system. Collaborative projects with industry and

Acknowledgements

The work at UCR was supported, in part, by the National Science Foundation (NSF) program Designing Materials to Revolutionize and Engineer our Future (DMREF) via a project DMR-1921958 entitled Collaborative Research: Data Driven Discovery of Synthesis Pathways and Distinguishing Electronic Phenomena of 1D van der Waals Bonded Solids. A. A. B. and T. D. acknowledge the support from the Vannevar Bush Faculty Fellowship from the Office of Secretary of Defense (OSD), under contract ONR-N00014-21-1-2947. The work at NRL was supported by the Office of Naval Research (ONR) through the Naval Research Laboratory's Basic Research Program. This work used the Extreme Science and Engineering Discovery Environment (XSEDE),60 which is supported by National Science Foundation grant number ACI-1053575 (1548562), allocation ID TG-DMR130081. A. A. B., L. B. and F. K. thank Evan Reed (Stanford University) for useful discussions on quasi-1D materials.

References

- 1 K. S. Novoselov, A. Mishchenko, A. Carvalho and A. H. Castro Neto, 2D Materials and van der Waals Heterostructures, Science, 2016, 353(6298), aac9439, DOI: 10.1126/science.aac9439.
- 2 A. K. Geim and I. V. Grigorieva, Van der Waals Heterostructures, Nature, 2013, 499(7459), 419-425, DOI: 10.1038/nature12385.
- 3 G. Liu, B. Debnath, T. R. Pope, T. T. Salguero, R. K. Lake and A. A. Balandin, A Charge-Density-Wave Oscillator Based on an Integrated Tantalum Disulfide-Boron Nitride-Graphene Device Operating at Room Temperature, Nat. 10.1038/ Nano., 2016, 11(10), NNANO.2016.108.
- 4 Q. H. Wang, K. Kalantar-Zadeh, A. Kis, J. N. Coleman and M. S. Strano, Electronics and Optoelectronics of Two-Dimensional Transition Metal Dichalcogenides, Nat. Nanotechnol., 2012, 699-712, DOI: 10.1038/nnano.2012.193.
- 5 D. Jariwala, V. K. Sangwan, L. J. Lauhon, T. J. Marks and M. C. Hersam, Emerging Device Applications for Semiconducting Two-Dimensional Transition Dichalcogenides, ACS Nano, 2014, 1102-1120, DOI: 10.1021/nn500064s.
- 6 A. C. Ferrari, F. Bonaccorso, V. Fal'Ko, K. S. Novoselov, S. Roche, P. Bøggild, S. Borini, F. H. L. Koppens, V. Palermo and N. Pugno, Science and Technology Roadmap for Graphene, Related Two-Dimensional Crystals, and Hybrid Systems, Nanoscale, 2015, 7(11), 4598-4810, DOI: 10.1039/ c4nr01600a.

7 K. S. Novoselov, A. K. Geim, S. V. Morozov, D. Jiang, Y. Zhang, S. V. Dubonos, I. V. Grigorieva and A. A. Firsov, Electric Field Effect in Atomically Thin Carbon Films, *Science*, 2004, 306(5696), 666–669, DOI: 10.1126/ science.1102896.

- 8 Y. Zhang, Y.-W. Tan, H. L. Stormer and P. Kim, Experimental Observation of the Quantum Hall Effect and Berry's Phase in Graphene, *Nature*, 2005, **438**(7065), 201–204, DOI: **10.1038/nature04235**.
- 9 A. A. Balandin, Thermal Properties of Graphene and Nanostructured Carbon Materials, *Nat. Mater.*, 2011, **10**(8), 569–581, DOI: **10.1038/nmat3064**.
- 10 L. Li, Y. Yu, G. J. Ye, Q. Ge, X. Ou, H. Wu, D. Feng, X. H. Chen and Y. Zhang, Black Phosphorus Field-Effect Transistors, *Nat. Nanotechnol.*, 2014, 9(5), 372–377, DOI: 10.1038/nnano.2014.35.
- 11 D. Teweldebrhan, V. Goyal and A. A. Balandin, Exfoliation and Characterization of Bismuth Telluride Atomic Quintuples and Quasi-Two-Dimensional Crystals, *Nano Lett.*, 2010, 10(4), 1209–1218, DOI: 10.1021/nl903590b.
- 12 B. Radisavljevic, A. Radenovic, J. Brivio, V. Giacometti and A. Kis, Single-Layer MoS₂ Transistors, *Nat. Nanotechnol.*, 2011, 6(3), 147–150, DOI: 10.1038/nnano.2010.279.
- 13 X. Cui, G.-H. Lee, Y. D. Kim, G. Arefe, P. Y. Huang, C.-H. Lee, D. A. Chenet, X. Zhang, L. Wang and F. Ye, Multi-Terminal Transport Measurements of MoS₂ Using a van Der Waals Heterostructure Device Platform, *Nat. Nanotechnol.*, 2015, 10(6), 534–540, DOI: 10.1038/nnano.2015.70.
- 14 S. Z. Butler, S. M. Hollen, L. Cao, Y. Cui, J. A. Gupta, H. R. Gutiérrez, T. F. Heinz, S. S. Hong, J. Huang, A. F. Ismach, E. Johnston-Halperin, M. Kuno, V. V. Plashnitsa, R. D. Robinson, R. S. Ruoff, S. Salahuddin, J. Shan, L. Shi, M. G. Spencer, M. Terrones, W. Windl and J. E. Goldberger, Progress, Challenges, and Opportunities in Two-Dimensional Materials beyond Graphene, ACS Nano, 2013, 7(4), 2898–2926, DOI: 10.1021/nn400280c.
- 15 A. Lipatov, P. M. Wilson, M. Shekhirev, J. D. Teeter, R. Netusil and A. Sinitskii, Few-Layered Titanium Trisulfide (TiS₃) Field-Effect Transistors, *Nanoscale*, 2015, 7(29), 12291–12296, DOI: 10.1039/c5nr01895a.
- 16 J. O. Island, M. Buscema, M. Barawi, J. M. Clamagirand, J. R. Ares, C. Sánchez, I. J. Ferrer, G. A. Steele, H. S. J. van der Zant and A. Castellanos-Gomez, Ultrahigh Photoresponse of Few-layer TiS₃ Nanoribbon Transistors, Adv. Opt. Mater., 2014, 2(7), 641–645, DOI: 10.1002/adom.201400043.
- 17 J. O. Island, M. Barawi, R. Biele, A. Almazán, J. M. Clamagirand, J. R. Ares, C. Sánchez, H. S. J. Van Der Zant, J. V. Álvarez, R. D'Agosta, I. J. Ferrer and A. Castellanos-Gomez, TiS₃ Transistors with Tailored Morphology and Electrical Properties, *Adv. Mater.*, 2015, 27(16), 2595–2601, DOI: 10.1002/adma.201405632.
- 18 M. A. Stolyarov, G. Liu, M. A. Bloodgood, E. Aytan, C. Jiang, R. Samnakay, T. T. Salguero, D. L. Nika, S. L. Rumyantsev, M. S. Shur, K. N. Bozhilov and A. A. Balandin, Breakdown

- Current Density in H-BN-Capped Quasi-1D TaSe₃ Metallic Nanowires: Prospects of Interconnect Applications, *Nanoscale*, 2016, 8(34), 15774–15782, DOI: 10.1039/C6NR03469A.
- M. Yamamoto, Superconducting Properties of TaSe₃,
 J. Phys. Soc. Jpn., 1978, 45(2), 431–438, DOI: 10.1143/
 JPSJ.45.431.
- 20 S. Nagata, S. Ebisu, T. Aochi, Y. Kinoshita, S. Chikazawa and K. Yamaya, Superconductivity in the Filamentary Conductor TaSe₃, *J. Phys. Chem. Solids*, 1991, 52(6), 761–767, DOI: 10.1016/0022-3697(91)90074-A.
- 21 E. Bjerkelund and A. Kjekshus, On the Crystal Structure of TaSe₃, *Acta Chem. Scand.*, 1965, **19**(3), 701–710.
- 22 E. Bjerkelund, J. H. Fermor and A. Kjekshus, On the Properties of TaS₃ and TaSe₃, *Acta Chem. Scand.*, 1966, 20(7), 1836–1842.
- 23 M. H. Rashid and D. J. Sellmyer, Electrical Conduction in Quasi-One-Dimensional Compounds: TaSe₃, Nb₂Se₃, and Nb₃S₄, *Phys. Rev. B: Condens. Matter Mater. Phys.*, 1984, **29**(4), 2359–2362, DOI: **10.1103/PhysRevB.29.2359**.
- 24 H. P. Geserich, G. Scheiber, F. Lévy and P. Monceau, Electrical Anisotropy of the Chain-like Conductors NbSe₃ and TaSe₃, *Phys. B+C*, 1986, 143(1-3), 174-176, DOI: 10.1016/0378-4363(86)90085-9.
- 25 A. Perucchi, C. Søndergaard, S. Mitrovic, M. Grioni, N. Barisic, H. Berger, L. Forró and L. Degiorg, Spectroscopic and DC-Transport Investigations of the Electronic Properties of TaSe₃, Eur. Phys. J. B, 2004, 39(4), 433–440, DOI: 10.1140/epjb/e2004-00214-x.
- 26 B. J. Kim, B. J. Jeong, S. Oh, S. Chae, K. H. Choi, T. Nasir, S. H. Lee, H. K. Lim, I. J. Choi, M.-K. Hong, H. K. Yu, J.-H. Lee and J.-Y. Choi, Thickness-Dependence Electrical Characterization of the One-Dimensional van der Waals TaSe₃ Crystal, *Materials*, 2019, 12(15), 2462, DOI: 10.3390/ma12152462.
- 27 J. Ma, S. Nie, X. Gui, M. Naamneh, J. Jandke, C. Xi, J. Zhang, T. Shang, Y. Xiong, I. Kapon, N. Kumar, Y. Soh, D. Gosálbez-Martínez, O. V. Yazyev, W. Fan, H. Hübener, U. D. Giovannini, N. C. Plumb, M. Radovic, M. A. Sentef, W. Xie, Z. Wang, C. Mudry, M. Müller and M. Shi, Multiple Mobile Excitons Manifested as Sidebands in Quasi-One-Dimensional Metallic TaSe₃, Nat. Mater., 2022, 21, 423–429, DOI: 10.1038/s41563-022-01201-9.
- 28 T. Sambongi, M. Yamamoto, K. Tsutsumi, Y. Shiozaki, K. Yamaya and Y. Abe, Superconductivity in One-Dimensional TaSe₃, *J. Phys. Soc. Jpn.*, 1977, 42(4), 1421–1422, DOI: 10.1143/JPSJ.42.1421.
- 29 P. Haen, F. Lapierre, P. Monceau, M. Núñez Regueiro and J. Richard, Low Temperature Phase Transition in the Chain-like Compounds NbSe₃ and TaSe₃, *Solid State Commun.*, 1978, 26(11), 725–730, DOI: 10.1016/0038-1098 (78)90729-9.
- 30 T. M. Tritt, E. P. Stillwell and M. J. Skove, Effect of Uniaxial Stress on the Transport Properties of TaSe₃, *Phys. Rev. B: Condens. Matter Mater. Phys.*, 1986, 34(10), 6799–6803, DOI: 10.1080/01411594.2016.1198963.

Paper Nanoscale

- 31 J.Á Silva-Guillén and E. Canadell, Strain Control of the Competition between Metallic and Semiconducting States in Single-Layers of TaSe₃, 2D Mater., 2020, 7(2), 025038, DOI: 10.1088/2053-1583/ab72d9.
- 32 S. Kikkawa, K. Shinya and M. Koizumi, The Selenide Systems of Niobium and Tantalum, I. Solid State Chem., 1982, 41(3), 323-328, DOI: 10.1016/0022-4596(82)90152-9.
- 33 J. Yang, Y. Q. Wang, R. R. Zhang, L. Ma, W. Liu, Z. Qu, L. Zhang, S. L. Zhang, W. Tong, L. Pi, W. K. Zhu and C. J. Zhang, Observation of Charge Density Wave Transition in TaSe₃ Mesowires, Appl. Phys. Lett., 2019, 115(3), 033102, DOI: 10.1063/1.5099110.
- 34 G. Kumagai, T. Matsuura, K. Ichimura and S. Tanda, Cylinder Vortex of Superconductor in TaSe₃ Topological Ring Crystals, in Journal of Physics: Conference Series, Institute of Physics Publishing, 2009, vol. 150, 052134, DOI: 10.1088/1742-6596/150/5/052134.
- 35 Y. Zhang, T. Zhu, H. Bu, Z. Cai, C. Xi, B. Chen, B. Wei, D. Lin, H. Xie, M. Naveed, X. Xi, F. Fei, H. Zhang and F. Song, Large Magnetoresistance in Topological Insulator Candidate TaSe₃, AIP Adv., 2020, 10(9), 095314, DOI: 10.1063/5.0015490.
- 36 E. Bjerkelund and A. Kjekshus, On the Properties of TaS₃, TaSe₃ and TaTe₄, ZAAC - J. Inorg. Gen. Chem., 1964, 328(5-6), 235-242, DOI: 10.1002/zaac.19643280506.
- 37 K. Yamaya and Y. Abe, Electrical Properties of Ta(S_xSe_{1-x})₃, Mol. Cryst. Liq. Cryst., 1982, 81(1), 133-140, DOI: 10.1080/ 00268948208072559.
- 38 J. Gill, Dislocations and the Motion of Weakly Pinned Charge-Density Waves: Experiments on Niobium Triselenide Containing Mobile Indium Impurities, Phys. Rev. B: Condens. Matter Mater. Phys., 1996, 53(23), 15586-15603, DOI: 10.1103/PhysRevB.53.15586.
- 39 A. V. Zavalko and S. V. Zaitsev-Zotov, Impurity-Induced Metal-Insulator Transition in Quasi-One-Dimensional Metals TaSe₃ and NbSe₃, J. Phys. IV, 2005, 131, 359-360, DOI: 10.1051/jp4:2005131093.
- 40 A. Nomura, K. Yamaya, S. Takayanagi, K. Ichimura and S. Tanda, Effect of Cu Doping on Superconductivity in TaSe₃: Relationship between Superconductivity and Induced Charge Density Wave, EPL (Europhysics Letters), 2019, 124(6), 67001, DOI: 10.1209/0295-5075/124/67001.
- 41 G. Cheon, K.-A. N. Duerloo, A. D. Sendek, C. Porter, Y. Chen and E. J. Reed, Data Mining for New Two- and One-Dimensional Weakly Bonded Solids and Lattice-Commensurate Heterostructures, Nano Lett., 2017, 17(3), 1915-1923, DOI: 10.1021/acs.nanolett.6b05229.
- 42 G. Cheon, E. D. Cubuk, E. R. Antoniuk, L. Blumberg, J. E. Goldberger and E. J. Reed, Revealing the Spectrum of Unknown Layered Materials with Superhuman Predictive Abilities, J. Phys. Chem. Lett., 2018, 9(24), 6967–6972, DOI: 10.1021/acs.jpclett.8b03187.
- 43 Z. Barani, F. Kargar, Y. Ghafouri, S. Baraghani, S. Sudhindra, A. Mohammadzadeh, T. T. Salguero and A. Balandin, Electromagnetic-Polarization-Selective Composites with Quasi-1D van der Waals Fillers:

- Nanoscale Material Functionality That Mimics Macroscopic Systems, ACS Appl. Mater. Interfaces, 2021, 13(18), 21527-21533, DOI: 10.1021/acsami.1c03204.
- 44 G. Liu, S. Rumyantsev, M. A. Bloodgood, T. T. Salguero, M. Shur and A. A. Balandin, Low-Frequency Electronic Noise in Quasi-1D TaSe₃ van der Waals Nanowires, Nano Lett., 2017, **17**(1), 377-383, DOI: 10.1021/acs. nanolett.6b04334.
- 45 M. Velický, A. Rodriguez, M. Bouša, A. V. Krayev, M. Vondráček, J. Honolka, M. Ahmadi, G. E. Donnelly, F. Huang, H. D. Abrunã, K. S. Novoselov and O. Frank, Strain and Charge Doping Fingerprints of the Strong Interaction between Monolayer MoS2 and Gold, J. Phys. Chem. Lett., 2020, 11(15), 6112-6118, DOI: 10.1021/acs. jpclett.0c01287.
- 46 T. P. Darlington, C. Carmesin, M. Florian, E. Yanev, O. Ajayi, J. Ardelean, D. A. Rhodes, A. Ghiotto, A. Krayev, K. Watanabe, T. Taniguchi, J. W. Kysar, A. N. Pasupathy, J. C. Hone, F. Jahnke, N. J. Borys and P. J. Schuck, Imaging Strain-Localized Excitons in Nanoscale Bubbles of Monolayer WSe₂ at Room Temperature, Nat. Nanotechnol., 2020, 15(10), 854-860, DOI: 10.1038/s41565-020-0730-5.
- 47 T. Debnath, B. Debnath and R. K. Lake, Thermal Conductivity of the Quasi-One-Dimensional Materials TaSe₃ and ZrTe₃, Phys. Rev. Mater., 2021, 5(3), 034010, DOI: 10.1103/PhysRevMaterials.5.034010.
- 48 B. A. Weinstein and G. J. Piermarini, Raman Scattering and Phonon Dispersion in Si and GaP at Very High Pressure, Phys. Rev. B: Condens. Matter Mater. Phys., 1975, 12(4), 1172-1186, DOI: 10.1103/PhysRevB.12.1172.
- 49 P. A. Temple and C. E. Hathaway, Multiphonon Raman Spectrum of Silicon, Phys. Rev. B: Condens. Matter Mater. DOI: Phys., 1973, 7(8), 3685-3697, 10.1103/ PhysRevB.7.3685.
- 50 J. H. Fan, P. Gao, A. M. Zhang, B. R. Zhu, H. L. Zeng, X. D. Cui, R. He and Q. M. Zhang, Resonance Raman Scattering in Bulk 2H-MX₂ (M = Mo, W; X = S, Se) and Monolayer MoS₂, J. Appl. Phys., 2014, 115(5), 53527, DOI: 10.1063/1.4862859.
- 51 A. Favron, F. A. Goudreault, V. Gosselin, J. Groulx, M. Côté, R. Leonelli, J. F. Germain, A. L. Phaneuf-L'Heureux, S. Francoeur and R. Martel, Second-Order Raman Scattering in Exfoliated Black Phosphorus, Nano Lett., 2018, 18(2), 1018-1027, DOI: 10.1021/acs.nanolett.7b04486.
- 52 T. J. Wieting, A. Grisel and F. Levy, Raman Scattering by Optical Phonons in TaSe₃ and NbSe₃, in Molecular crystals and liquid crystals; Taylor & Francis Group, 1982, vol. 81, pp. 117-124. DOI: 10.1080/00268948208072557.
- 53 P. Hohenberg and W. Kohn, Inhomogeneous Electron Gas, Phys. Rev., 1964, 136(3B), B864, DOI: 10.1103/PhysRev.136. B864.
- 54 W. Kohn and L. J. Sham, Self-Consistent Equations Including Exchange and Correlation Effects, Phys. Rev., 1965, 140(4A), A1133, DOI: 10.1103/PhysRev.140.A1133.
- 55 G. Kresse and J. Furthmüller, Efficiency of Ab initio Total Energy Calculations for Metals and Semiconductors Using

a Plane-Wave Basis Set, *Comput. Mater. Sci.*, 1996, **6**(1), 15–50, DOI: **10.1016/0927-0256(96)00008-0**.

- A. Hjorth Larsen, J. Jørgen Mortensen, J. Blomqvist, I. E. Castelli, R. Christensen, M. Dułak, J. Friis, M. N. Groves, B. Hammer, C. Hargus, E. D. Hermes, P. C. Jennings, P. Bjerre Jensen, J. Kermode, J. R. Kitchin, E. Leonhard Kolsbjerg, J. Kubal, K. Kaasbjerg, S. Lysgaard, J. Bergmann Maronsson, T. Maxson, T. Olsen, L. Pastewka, A. Peterson, C. Rostgaard, J. SchiØtz, O. Schütt, M. Strange, K. S. Thygesen, T. Vegge, L. Vilhelmsen, M. Walter, Z. Zeng and K. W. Jacobsen, The Atomic Simulation Environment —a Python Library for Working with Atoms, J. Phys.: Condens. Matter, 2017, 29(27), 273002, DOI: 10.1088/1361-648X/AA680E.
- 57 J. P. Perdew, K. Burke and M. Ernzerhof, Generalized Gradient Approximation Made Simple, *Phys. Rev. Lett.*,

- 1996, 77(18), 3865–3868, DOI: **10.1103/ PhysRevLett.77.3865.**
- 58 S. Grimme, Semiempirical GGA-Type Density Functional Constructed with a Long-Range Dispersion Correction, *J. Comput. Chem.*, 2006, 27(15), 1787–1799, DOI: 10.1002/jcc.20495.
- 59 C. S. Cucinotta, K. Dolui, H. Pettersson, Q. M. Ramasse, E. Long, S. E. O'Brian, V. Nicolosi and S. Sanvito, Electronic Properties and Chemical Reactivity of TiS₂ Nanoflakes, J. Phys. Chem. C, 2015, 119(27), 15707–15715, DOI: 10.1021/ acs.jpcc.5b03212.
- 60 J. Towns, T. Cockerill, M. Dahan, I. Foster, K. Gaither, A. Grimshaw, V. Hazlewood, S. Lathrop, D. Lifka, G. D. Peterson, R. Roskies, J. R. Scott and N. Wilkens-Diehr, XSEDE: Accelerating Scientific Discovery, *Comput. Sci. Eng.*, 2014, 16(5), 62–74, DOI: 10.1109/MCSE.2014.80.